Supplementrary material: Using 3D Topological Connectivity for Ghost Particle Reduction in Flow Reconstruction

Christina Tsalicoglou Thomas Rösgen
Institute of Fluid Dynamics, ETH Zurich
Zurich, Switzerland
{ctsalico,roesgen}@ethz.ch

1. Ghost streak generation probablities

1.1. Linear streaks

The average areas of intersection $f_{s,R}$, f_A, f_B and f_C, used in the calculations for the generation probability of ghost streaks with bounded displacements are described below. We provide the result of the integration where the resulting formula is short. Otherwise we chose to leave the integrals, which better elucidate the reasoning behind the derivation of the results.

1.1.1 Intersection area $f_{s,R}$

$\bar{f}_{s,R}$ is split into 4 regions:
If $R = 0$, $\bar{f}_{s,R} = 0$
If $0 < R \leq d$

$$\begin{aligned}\bar{f}_{s,R} = \frac{4}{\pi R^2 d}\int_0^R \sqrt{R^2-\hat{y}^2} \quad & \left(\int_{-d}^{-d+\hat{y}+R}\int_{-d+\hat{y}-z}^{R} \sqrt{R^2-\hat{z}^2}\,d\hat{z}\,dz \right. \\ & + \frac{1}{2}\int_{-d+\hat{y}+R}^{d+\hat{y}-R} \pi R^2\,dz \\ & \left. + \int_{d+\hat{y}-R}^{d}\int_{-R}^{d+\hat{y}-z} \sqrt{R^2-\hat{z}^2}\,d\hat{z}\,dz \right) d\hat{y} \\ = \frac{4}{\pi R^2 d}\left(\frac{1}{4}\pi^2 d R^4 - \frac{32R^5}{45}\right) &\end{aligned} \tag{1}$$

If $d < R \leq 2d$

$$\begin{aligned}\bar{f}_{s,R} = \frac{4}{\pi R^2 d}\Bigg(& \int_0^{2d-R} \sqrt{R^2-\hat{y}^2}\Bigg(\int_{-d}^{d+\hat{y}-R}\int_{\hat{y}-d-z}^{R} \sqrt{R^2-\hat{z}^2}\,d\hat{z}\,dz \\ & + \int_{d+\hat{y}-R}^{\hat{y}-d+R}\int_{\hat{y}-d-z}^{\hat{y}+d-z} \sqrt{R^2-\hat{z}^2}\,d\hat{z}\,dz \\ & + \int_{\hat{y}-d+R}^{d}\int_{-R}^{\hat{y}+d-z} \sqrt{R^2-\hat{z}^2}\,d\hat{z}\,dz \Bigg) d\hat{y} \\ & + \int_{2d-R}^{R} \sqrt{R^2-\hat{y}^2}\Bigg(\int_{-d}^{d+\hat{y}-R}\int_{\hat{y}-d-z}^{R} \sqrt{R^2-\hat{z}^2}\,d\hat{z}\,dz \\ & + \int_{d+\hat{y}-R}^{d}\int_{\hat{y}-d-z}^{\hat{y}+d-z} \sqrt{R^2-\hat{z}^2}\,d\hat{z}\,dz \Bigg) d\hat{y} \Bigg)\end{aligned} \tag{2}$$

If $R > 2d$

$$\bar{f}_{s,R} = \frac{4}{\pi R^2 d}\Bigg(\int_0^{R-2d} \sqrt{R^2-\hat{y}^2} \int_{-d}^{d} \int_{\hat{y}-d-z}^{\hat{y}+d-z} \sqrt{R^2-\hat{z}^2}\, d\hat{z}\, dz\, d\hat{y} + \int_{R-2d}^{R} \sqrt{R^2-\hat{y}^2} \int_{-d}^{d+\hat{y}-R} \int_{\hat{y}-d-z}^{R} \sqrt{R^2-\hat{z}^2}\, d\hat{z}\, dz\, d\hat{y} + \int_{R-2d}^{R} \sqrt{R^2-\hat{y}^2} \int_{d+\hat{y}-R}^{d} \int_{\hat{y}-d-z}^{\hat{y}+d-z} \sqrt{R^2-\hat{z}^2}\, d\hat{z}\, dz\, d\hat{y} \Bigg) \tag{3}$$

1.1.2 Intersection area f_A

The mean product of the two areas $f_A(z)$ is split into 3 regions:

If $R = 0$, $\bar{f}_A^2 = 0$

If $0 < R \leq 2d$

$$\bar{f}_A^2 = \frac{1}{R} \int_0^R \int_z^R \sqrt{R^2-\hat{y}^2} \int_{-R}^{-z} \sqrt{R^2-\hat{z}^2}\, d\hat{z}\, d\hat{y}\, dz = \frac{1}{90}(15\pi - 32)R^4 \tag{4}$$

If $R > 2d$

$$\bar{f}_A^2 = \frac{1}{R}\Bigg(\int_0^{R-2d} \int_z^{z+2d} \sqrt{R^2-\hat{y}^2} \int_{-z-2d}^{-z} \sqrt{R^2-\hat{z}^2}\, d\hat{z}\, d\hat{y}\, dz + \int_{R-2d}^{R} \int_z^R \sqrt{R^2-\hat{y}^2} \int_{-R}^{-z} \sqrt{R^2-\hat{z}^2}\, d\hat{z}\, d\hat{y}\, dz \Bigg) \tag{5}$$

1.1.3 Intersection area f_B

$\bar{f}_B$ is split into 4 regions:

If $R = 0$, $\bar{f}_B = 0$

If $0 < R \leq d$

$$\bar{f}_B = \frac{4}{\pi R^2 d} \int_0^R \sqrt{R^2-\hat{y}^2}\Bigg(\int_{-d+\hat{y}}^{-d+R} \int_{-d-z}^{-d+\hat{y}-z} \sqrt{R^2-\hat{z}^2}\, d\hat{z}\, dz + \int_{-d+R}^{-d+\hat{y}+R} \int_{-R}^{-d+\hat{y}-z} \sqrt{R^2-\hat{z}^2}\, d\hat{z}\, dz \Bigg) d\hat{y} \tag{6}$$

If $d < R \leq 2d$

$$\bar{f}_B = \frac{4}{\pi R^2 d}\Bigg(\int_0^{2d-R} \sqrt{R^2-\hat{y}^2}\Bigg(\int_{-d+\hat{y}}^{-d+R} \int_{-d-z}^{-d+\hat{y}-z} \sqrt{R^2-\hat{z}^2}\, d\hat{z}\, dz + \int_{-d+R}^{-d+\hat{y}+R} \int_{-R}^{-d+\hat{y}-z} \sqrt{R^2-\hat{z}^2}\, d\hat{z}\, dz \Bigg) d\hat{y} + \int_{2d-R}^{R} \sqrt{R^2-\hat{y}^2}\Bigg(\int_{-d+\hat{y}}^{-d+R} \int_{-d-z}^{-d+\hat{y}-z} \sqrt{R^2-\hat{z}^2}\, d\hat{z}\, dz + \int_{-d+R}^{d} \int_{-R}^{-d+\hat{y}-z} \sqrt{R^2-\hat{z}^2}\, d\hat{z}\, dz \Bigg) d\hat{y} \Bigg) \tag{7}$$

If $R > 2d$

$$\bar{f}_B = \frac{4}{\pi R^2 d} \int_0^{2d} \sqrt{R^2-\hat{y}^2} \int_{-d+\hat{y}}^{d} \int_{-d-z}^{-d+\hat{y}-z} \sqrt{R^2-\hat{z}^2}\, d\hat{z}\, dz\, d\hat{y} \tag{8}$$

1.1.4 Intersection area f_C

$\bar{f}_C$ is split into 5 regions:

If $R = 0$, $\bar{f}_C = 0$

If $0 < R \leq 2d/3$

$$\begin{aligned}\bar{f}_C = \frac{4}{\pi R^2 d}\int_0^R \sqrt{R^2-\hat{y}^2}\Bigg(&\int_{-d+\hat{y}}^{-d+\hat{y}+R}\int_{-d+\hat{y}-z}^{R}\sqrt{R^2-\hat{z}^2}\,d\hat{z}\,dz \\ &+\int_{-d+\hat{y}+R}^{d-R}\int_{-R}^{R}\sqrt{R^2-\hat{z}^2}\,d\hat{z}\,dz \\ &+\int_{d-R}^{d}\int_{R}^{d-z}\sqrt{R^2-\hat{z}^2}\,d\hat{z}\,dz\Bigg)d\hat{y}\end{aligned} \tag{9}$$

If $2d/3 < R \leq d$

$$\begin{aligned}\bar{f}_C = \frac{4}{\pi R^2 d}\Bigg(&\int_0^{2d-2R}\sqrt{R^2-\hat{y}^2}\Bigg(\int_{-d+\hat{y}}^{-d+\hat{y}+R}\int_{-d+\hat{y}-z}^{R}\sqrt{R^2-\hat{z}^2}\,d\hat{z}\,dz \\ &+\int_{-d+\hat{y}+R}^{d-R}\int_{-R}^{R}\sqrt{R^2-\hat{z}^2}\,d\hat{z}\,dz \\ &+\int_{d-R}^{d}\int_{-R}^{d-z}\sqrt{R^2-\hat{z}^2}\,d\hat{z}\,dz\Bigg)d\hat{y} \\ &+\int_{2d-2R}^{R}\sqrt{R^2-\hat{y}^2}\Bigg(\int_{-d+\hat{y}}^{d-R}\int_{-d+\hat{y}-z}^{R}\sqrt{R^2-\hat{z}^2}\,d\hat{z}\,dz \\ &+\int_{d-R}^{-d+\hat{y}+R}\int_{-d+\hat{y}-z}^{d-z}\sqrt{R^2-\hat{z}^2}\,d\hat{z}\,dz \\ &+\int_{-d+\hat{y}+R}^{d}\int_{-R}^{d-z}\sqrt{R^2-\hat{z}^2}\,d\hat{z}\,dz\Bigg)d\hat{y}\Bigg)\end{aligned} \tag{10}$$

If $d < R \leq 2d$

$$\begin{aligned}\bar{f}_C = \frac{4}{\pi R^2 d}\Bigg(&\int_0^{2d-2R}\sqrt{R^2-\hat{y}^2}\Bigg(\int_{-d+\hat{y}}^{d-R}\int_{-d+\hat{y}-z}^{R}\sqrt{R^2-\hat{z}^2}\,d\hat{z}\,dz \\ &+\int_{d-R}^{-d+\hat{y}+R}\int_{-d+\hat{y}-z}^{d-z}\sqrt{R^2-\hat{z}^2}\,d\hat{z}\,dz \\ &+\int_{-d+\hat{y}+R}^{d}\int_{-R}^{d-z}\sqrt{R^2-\hat{z}^2}\,d\hat{z}\,dz\Bigg)d\hat{y} \\ &+\int_{2d-2R}^{R}\sqrt{R^2-\hat{y}^2}\int_{-d+\hat{y}}^{d}\int_{-d+\hat{y}-z}^{d-z}\sqrt{R^2-\hat{z}^2}\,d\hat{z}\,dz\,d\hat{y}\Bigg)\end{aligned} \tag{11}$$

If $R > 2d$

$$\bar{f}_C = \frac{4}{\pi R^2 d}\int_0^{2d}\sqrt{R^2-\hat{y}^2}\int_{-d+\hat{y}}^{d}\int_{-d+\hat{y}-z}^{d-z}\sqrt{R^2-\hat{z}^2}\,d\hat{z}\,dz\,d\hat{y} \tag{12}$$

1.2. Ellipse segments

The formulae for the calculation of the ghost ellipse generation probability, $\bar{p}_e$, are presented below. They hold for $d_e < H/2 - 2R$ and $d \ll R$.

The probability that one of the ellipse's tangents will be in the desired region is

$$\bar{p}_{z_2}(y,\hat{y}) = \frac{1}{(H+R-y-\hat{y}/2)^2}\left(\int_{y+\hat{y}/2}^{y+\hat{y}/2+d_e}(d_e+z_2-y-\hat{y}/2)\,dz_2 + \int_{y+\hat{y}/2+d_e}^{H+R-d_e} 2d_e\,dz_2 + \int_{H+R-d_e}^{H+R}(d_e+H+R-z_2)\,dz_2\right) \tag{13}$$

Then the mean probability that both of the ellipse's tangents will be in the desired region is:

$$\begin{aligned}\bar{p}_e = \frac{4}{\pi R^2}\int_0^R \frac{\sqrt{R^2-\hat{y}^2}}{H/2-\hat{y}/2}\Bigg(&\int_{\hat{y}/2}^{d_e-R+\hat{y}/2}\frac{\bar{p}_{z_2}(y,\hat{y})}{R+y-\hat{y}/2}\int_{-R}^{y-\hat{y}/2}dz_1\,dy \\ &+\int_{d_e-R+\hat{y}/2}^{2d_e-R+\hat{y}/2}\frac{\bar{p}_{z_2}(y,\hat{y})}{R+y-\hat{y}/2}\Bigg(\int_{-R}^{y-\hat{y}/2-d_e}\frac{d_e+z_1+R}{R+y-\hat{y}/2}\,dz_1 \\ &\qquad+\int_{y-\hat{y}/2-d_e}^{d_e-R}dz_1 \\ &\qquad+\int_{d_e-R}^{y-\hat{y}/2}\frac{d_e+y-\hat{y}/2-z_1}{R+y-\hat{y}/2}\,dz_1\Bigg)dy \\ &+\int_{2d_e-R+\hat{y}/2}^{H/2}\frac{\bar{p}_{z_2}(y,\hat{y})}{R+y-\hat{y}/2}\Bigg(\int_{-R}^{d_e-R}\frac{d_e+z_1+R}{R+y-\hat{y}/2}\,dz_1 \\ &\qquad+\int_{d_e-R}^{y-\hat{y}/2-d_e}\frac{2d_e}{R+y-\hat{y}/2}\,dz_1 \\ &\qquad+\int_{y-\hat{y}/2-d_e}^{y-\hat{y}/2}\frac{d_e+y-\hat{y}/2-z_1}{R+y-\hat{y}/2}\,dz_1\Bigg)dy\Bigg)d\hat{y}\end{aligned} \tag{14}$$

2. RANSAC-based conic matching and reconstruction method

The method that is used as a baseline is a RANSAC-based approach that iteratively selects a new subset of the datapoints to perform the conic fits and then uses the epipolar transfer method described by [6] to evaluate whether the examined conic section segments are valid matches. We implement this approach for two and three cameras. Additional cameras would have to be evaluated in triplets.

At every iteration step, a subset of the datapoints that define the conic segments in two images is selected, and new conic sections C and C′ are fitted to those points. The criterion for conic matching is whether there exists a homography that transforms one conic into the other and, therefore, whether there exists a plane on which the world conic lies that is projected to the camera views. [6] proposed using the polar lines of two putatively corresponding conics to constrain the search for the plane-induced homography, as the polar lines of corresponding conics also correspond, due to the epipolar tangency constraint. Here, this algorithm is modified to account for the fact that the streak endpoints provide a line correspondence condition.

With a sufficiently good approximation of the two conics, C and C′, the polar-based method produces good results. However, our estimates of the conics to which the streak segments belong are usually poor due to the segments' low curvature and short lengths. We use the fact that due to prior evaluation, we know that the endpoints of the streaks correspond, and, therefore, the two lines that pass through the streaks' endpoints in the two images correspond. Consequently, we use the line that defines the streak endpoints as the axis of the pencil of planes of which the desired plane of the conic is a member.

As described by [6], a family of homographies, provided two line correspondences $\mathbf{l}$ and $\mathbf{l}'$ is given by:

$$\mathrm{H}(\mu) = [\mathbf{l}']_\times \mathrm{F} + \mu \mathbf{e}'\mathbf{l}^\top. \tag{15}$$

We define the following, as it is known that the endpoints of the streaks, $\mathbf{x_s}$, $\mathbf{x_e}$ and $\mathbf{x}'_\mathbf{s}$, $\mathbf{x}'_\mathbf{e}$ correspond.

$$\mathbf{l} = [\mathbf{x_s}]_\times \mathbf{x}_e, \tag{16}$$
$$\mathbf{l}' = [\mathbf{x}'_\mathbf{s}]_\times \mathbf{x}'_e, \tag{17}$$
$$\mathrm{K}_1 = [\mathbf{l}']_\times \mathrm{F}, \tag{18}$$
$$\mathrm{K}_2 = \mathbf{e}'\mathbf{l}^\top, \tag{19}$$
$$\mathrm{H}(\mu) = \mathrm{K}_1 + \mu \mathrm{K}_2. \tag{20}$$

A conic C' then transforms to C, given the homography H between the conic' planes:

$$\mathrm{C} = \mathrm{H}^\top \mathrm{C}' \mathrm{H}. \tag{21}$$

This is a homogeneous equation so it contains a hidden scale factor γ

$$\begin{aligned} \gamma \mathrm{C} &= [{\mathrm{K}_1}^\top + \mu {\mathrm{K}_2}^\top] \mathrm{C}' [\mathrm{K}_1 + \mu \mathrm{K}_2] \\ &= \mu^2 {\mathrm{K}_2}^\top \mathrm{C}' \mathrm{K}_2 + \mu [{\mathrm{K}_2}^\top \mathrm{C}' \mathrm{K}_1 + {\mathrm{K}_1}^\top \mathrm{C}' \mathrm{K}_2] + {\mathrm{K}_1}^\top \mathrm{C}' \mathrm{K}_1 \end{aligned} \tag{22}$$

We define

$$\begin{aligned} \mathrm{M_A} &= {\mathrm{K}_2}^\top \mathrm{C}' \mathrm{K}_2, \\ &= \mathbf{l}{\mathbf{e}'}^\top \mathrm{C}' \mathbf{e}' \mathbf{l}^\top \end{aligned} \tag{23}$$
$$\begin{aligned} \mathrm{M_B} &= {\mathrm{K}_2}^\top \mathrm{C}' \mathrm{K}_1 + {\mathrm{K}_1}^\top \mathrm{C}' \mathrm{K}_2, \\ &= \mathbf{l}{\mathbf{e}'}^\top \mathrm{C}' [\mathbf{l}']_\times \mathrm{F} - \mathrm{F}^\top [\mathbf{l}']_\times \mathrm{C}' \mathbf{e}' \mathbf{l}^\top \end{aligned} \tag{24}$$
$$\begin{aligned} \mathrm{M_C} &= {\mathrm{K}_1}^\top \mathrm{C}' \mathrm{K}_1, \\ &= -\mathrm{F}^\top [\mathbf{l}']_\times \mathrm{C}' [\mathbf{l}']_\times \mathrm{F} \end{aligned} \tag{25}$$

Multiplying both sides with the epipole $\mathbf{e}$ simplifies the equation, as $\mathrm{F}\mathbf{e} = 0$

$$\begin{aligned} \gamma \mathbf{e}^\top \mathrm{C} \mathbf{e} &= \mu^2 \mathbf{e}^\top \mathrm{M_A} \mathbf{e} \\ \Rightarrow \gamma &= \mu^2 \frac{s_{M_A}}{s_C} \end{aligned} \tag{26}$$

with the scalars s_C and $s_{\mathrm{M_A}}$ being

$$s_\mathrm{C} = \mathbf{e}^\top \mathrm{C} \mathbf{e}, \tag{27}$$
$$s_{\mathrm{M_A}} = \mathbf{e}^\top \mathrm{M_A} \mathbf{e} \tag{28}$$

Substituting γ in Eq. 22

$$\begin{aligned} \mu^2 \frac{s_{\mathrm{M_A}}}{s_\mathrm{C}} \mathrm{C} =& \mu^2 \mathrm{M_A} + \mu \mathrm{M_B} + \mathrm{M_C} \\ \Rightarrow& \mu^2 [\mathrm{M_A} - \frac{s_{\mathrm{M_A}}}{s_\mathrm{C}} \mathrm{C}] + \mu \mathrm{M_B} + \mathrm{M_C} = 0 \end{aligned} \tag{29}$$
$$a = [\mathrm{M_A} - \frac{s_{\mathrm{M_A}}}{s_\mathrm{C}} \mathrm{C}] \tag{30}$$
$$b = \mathrm{M_B} \tag{31}$$
$$c = \mathrm{M_C} \tag{32}$$

The terms a, b, c, are matrices so the solution that best satisfies all elements of the equation $\mathrm{C} = \mathrm{H}^\top \mathrm{C}'\mathrm{H}$ will be found when the sum of squares of the components of the matrix of differences $\gamma\mathrm{C} - \mathrm{H}^\top \mathrm{C}'\mathrm{H}$ is minimized. Therefore:

$$\begin{aligned} &\min \sum_{ij} \left(\gamma \mathrm{C}_{ij} - [\mathrm{H}^\top \mathrm{C}'\mathrm{H}]_{ij}\right)^2 \\ \Rightarrow &\min \sum_{ij} (\mu^2 a_{ij} + \mu b_{ij} + c_{ij})^2 \end{aligned} \tag{33}$$

We set the derivative w.r.t. μ to zero to find the local extrema of the function. Then we solve a third order polynomial, which has a closed-form solution, and do the second derivative test to only select solutions that describe local minima.

$$\begin{aligned} &\frac{\partial}{\partial \mu} \sum_{ij} (\mu^2 a_{ij} + \mu b_{ij} + c_{ij})^2 = 0 \\ \Rightarrow &\sum_{ij} (2\mu^3 a_{ij}^2 + 3\mu^2 a_{ij} b_{ij} + \mu(b_{ij}^2 + 2a_{ij}c_{ij}) + b_{ij}c_{ij}) = 0. \end{aligned} \tag{34}$$

Once the solution for μ is found, the homography can be found using Eq. 15. By transforming the points from I to I' and calculating the mean distance of the transformed point cloud to the original fitted conic, the quality of the transfer, and, therefore, the match, can be quantified.

When three cameras are used, the points from I are transferred to I'' through the now known plane that results in the derived homography $\mathrm{H}(\mu)$ and the fit criterion is how well the transferred points fit the conic on I''. The fit criterion is defined in the same way as in the optimization-based case. Finally, the test can be performed in pair-wise fashion between different sets of cameras.

For the results presented in the paper, and for each RANSAC iteration, we sample 10 points of the 80 comprising each conic section segment to estimate a conic fit. We use more points than the minimum 5 needed because we assume that all our points are inliers and our data is noisy, so we use a RANSAC approach to get a variety of fits through the datapoints rather than to perform an inlier-outlier detection. We generate 20 fits for each view, from which we estimate the plane on which the 3D conic might lie, as described above.

3. Regularizer for noisy data

When the datapoints defining the conic section segments are noisy, as in experimental data, the optimization problem sometimes fits a hyperbola with an eccentricity close to one, producing conic segments with sharp turns to fit some outliers. Such fits are rarely suitable for streak images, where the fitted conic section segments represent particle trajectories. Therefore, in such cases, we use a regularizer, R_i, that penalizes conic sections with an eccentricity close to one:

$$R_i(\boldsymbol{\pi}, \theta_{\boldsymbol{\pi}}) = \frac{1}{(1 - e_i^2)^2}, \tag{35}$$

where e_i is the eccentricity of each of the projected conic sections [2]. Leading to the regularized objective function

$$\mathcal{L}_R(\boldsymbol{\pi}, \theta_{\boldsymbol{\pi}}) = \sum_{i,j} \frac{(\mathbf{x}_{i,j}^\top \mathrm{C}_i \mathbf{x}_{i,j})^2}{4((\mathrm{C}_i \mathbf{x}_{i,j})_1^2 + (\mathrm{C}_i \mathbf{x}_{i,j})_2^2)} + \lambda \sum_i R_i(\boldsymbol{\pi}, \theta_{\boldsymbol{\pi}})\,. \tag{36}$$

4. Validation datasets and evaluation

4.1. Conic section data

The mean streak length for the conic section data presented in Section 4.2.1 of the main paper is 18 px. An example of the used images can be seen in Fig. 1. A comparison of the data of Table 2 of the main paper with the models can be seen in Fig. 2. For the comparison to the model we use R = 27 px, as, if we assume uniform distribution of the streaks' endpoints within a circle with R = 27 px, the mean radius is 18 px, which is the mean displacement in our synthetic data. Additionally,

for the curved streak model we use an epipolar constraint tolerance d_e = 200 px, which fits best with the data. Using a different tolerance would result in a different prediction for the number of ambiguities, but it is important to see that the trend of the simulated data follows that of the model. The image size is 1024×1024 px^2.

With the same data we also perform 3-camera reconstruction, and the results can be seen in Table 1. On this table we show the results from one run for a single 3D-scene, instead of the average of 20 scenes as in the rest of the paper.

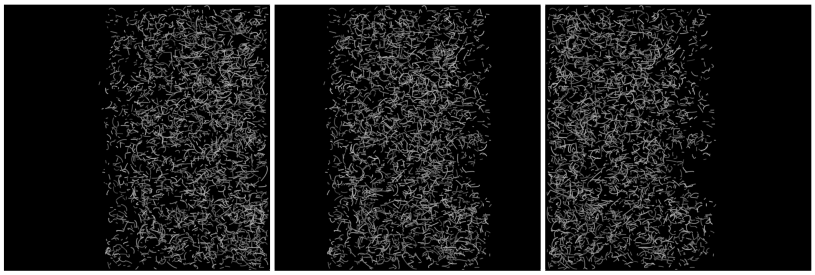

Figure 1. Example of the synthetic conic section data used for the validation of the conic section reconstruction method.

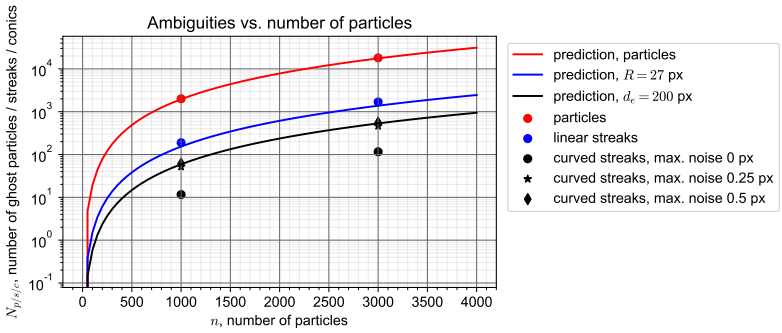

Figure 2. Comparison of the ghost particles, linear streaks and curved streaks with the models. The markers correspond to the data provided in Table 2 of the main paper, while the lines are the model predictions.

	N_p	N_s	N_c, optimization	
	ghosts	ghosts	ghosts	lost
	0 px			
n=1000	76.5	0	0	0
	7.7%	0%	0%	0%
n=3000	878	8	0	0
	29.3%	0.27%	0%	0%
	0.25 px			
n=1000	68	0	0	0
	6.8%	0%	0%	0%
n=3000	848.5	7	0	2
	28.3%	0.23%	0%	0.07%
	0.5 px			
n=1000	65	0	0	0
	6.5%	0%	0%	0%
n=3000	787	4	1	0
	26.2%	0.13%	0.03%	0%

Table 1. Reconstruction results using 3 cameras, showing the number of reconstructed individual ghost particles, N_p, ghost streaks, N_s, and curved ghost streaks, N_c, for different initial numbers of particles n and different noise levels, for the case of random conic section data. "Ghosts" are the ambiguous reconstructions, while "lost" are the false negatives, which result in losing correct matches during the reconstruction process.

4.2. Hill's spherical vortex data

The distribution of the particle displacements for the case of Hill's spherical vortex can be seen in Fig. 3 for an image with 3000 particles. The resulting images for 1000 and 3000 particle images can be seen in Fig. 4. The streamlines for Hill's spherical vortex can be seen in Figs. 5a and 5b together with our reconstruction of the streaks 5c.

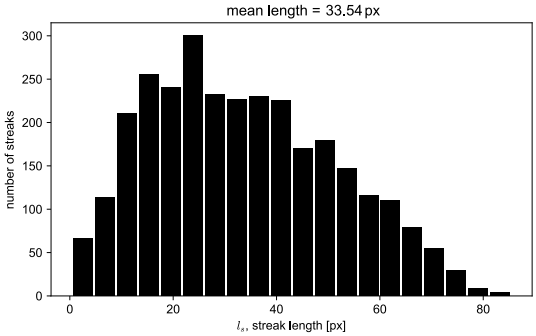

Figure 3. Distribution of streak lengths for the case with 3000 particles in the image.

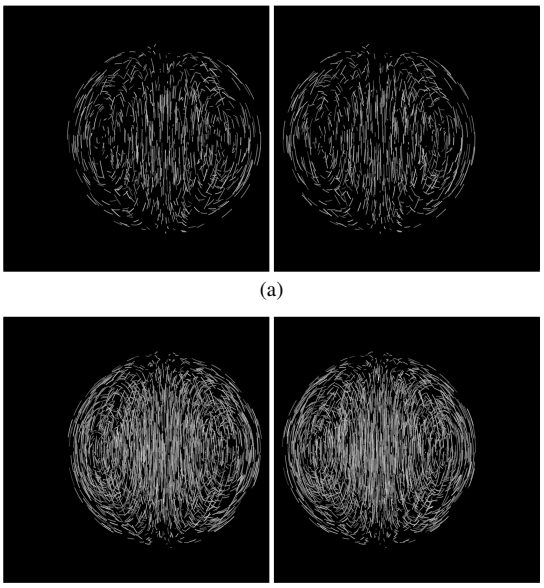

(a)

(b)

Figure 4. Example of the synthetic data based on Hill's spherical vortex imaged on two views for (a) 1000 particles and (b) 3000 particles.

4.3. Settings for the 3D-PTV commercial software

For the comparison with a commercial 3D-PTV type software [4], we extract particle images from every 10th timestep of each streak image, resulting in 10 timesteps to be processed with the 3D-PTV software. The settings used for the results presented are:

- Allowed triangulation error: 1 voxel
- Minimum track length required: 6 timesteps
- Threshold for 2D particle detection: 1000 counts
- Voxel to mm ratio: 1800 voxels correspond to 600 mm

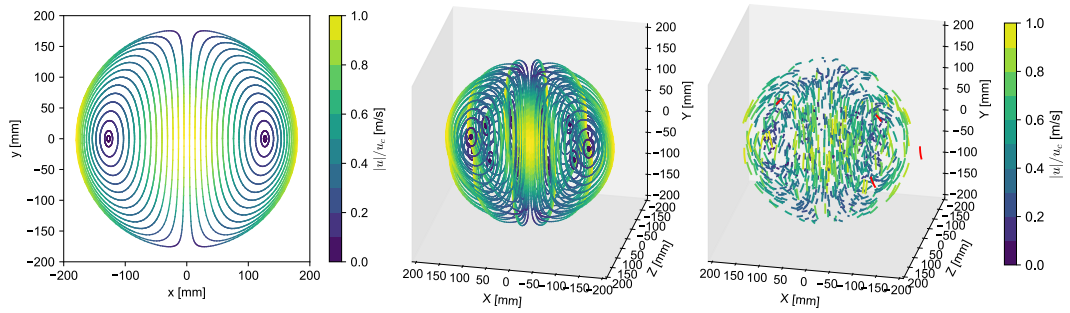

(a) (b) (c)

Figure 5. (a) Streamlines of a 2D slice of the rotationally symmetric Hill's spherical vortex and (b) 3D streamlines, colored by the normalized absolute velocity, where u_c is the maximum speed, at the center of the sphere. (c) Reconstructed streaks originating from the same flow field as the images of Fig. 4a, with the ghost streaks shown in red.

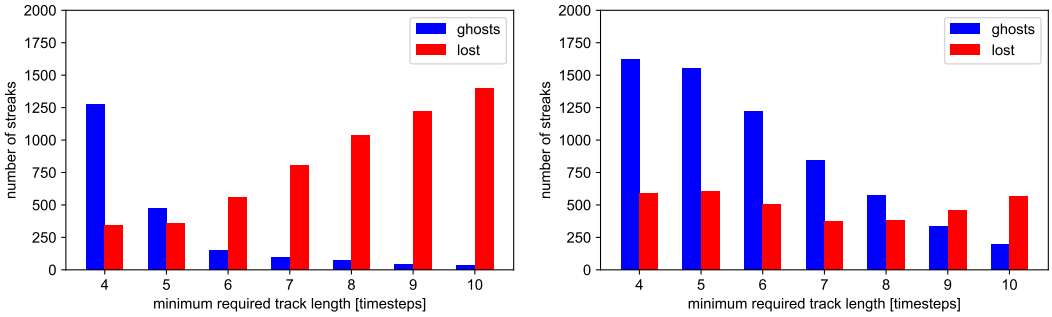

(a) (b)

Figure 6. Number of reconstructed ghost tracks and lost tracks, for an initial number of particles n = 3000 in each image and for (a) 10 frames with a mean displacement of 3.3 px and (b) 20 frames with a mean displacement of 1.7 px. The results presented in the paper correspond to subfigure (a) with a minimum required track length of 6 timesteps.

Wherever not specified, the default settings were used.

The same synthetic calibration as we use for the evaluation with our method was introduced in DaVis. After volume self-calibration we obtain a fit error of 0.0026 px. On the images, the particles appear as Gaussian blobs with different intensities that are consistent across views and for multiple timesteps, as this produced better results than constant intensities.

With our settings, the mean particle displacement per frame is 3.3 px and the maximum displacement is around 8px. We also performed tests with smaller particle displacements of a mean of 1.7 px and maximum of 4 px. The obtained results are presented in Fig. 6 for the case with 3000 particles. We chose the settings based on the 3000 particle case and used the same settings for 1000 particles.

4.4. Results without volume and velocity constraints

The results presented in the paper for the case of Hill's spherical vortex are valid reconstructions within a volume of $600\times600\times600$ mm centered around the sphere, with a constrained velocity, so that we can make a fair comparison between our results and the results obtained using the commercial software. Below, we present the results for an unconstrained reconstruction volume and particle velocity, so that we can compare the number of resulting ghost streaks with our theoretical estimates. The numbers of ghost particles, linear streaks and conic section segments is larger than in our ideal cases, as the flow does not follow our assumptions. Still, significantly fewer ghost streaks are reconstructed, compared to particles.

5. Experiment

For the experiments, we use two Photron AX100 high-speed cameras arranged around a vortex ring generator. The camera resolution is 1024×1024 px with a pixel size of 20 μm, and we use 55 mm Micro-Nikkor Nikon lenses. The measurement volume is illuminated by a continuous 50 W white LED light source and the light is collimated by a Fresnel lens (Fig. 7). Our

	N_p	N_s	N_c, optimization	
	ghosts	ghosts	ghosts	lost
	0 px			
n=1000	3109	84	45	0
	310.9%	8.4%	4.5%	0%
n=3000	29112	934	482	0
	970.4%	31.1%	16.1%	0%
	0.25 px			
n=1000	3129.5	89	82	5
	313%	8.9%	8.2%	0.5%
n=3000	29204	923	772	41
	973.5%	30.8%	25.7%	1.4%
	0.5 px			
n=1000	3133.5	102	97	3
	313.4%	10.2%	9.7%	0.3%
n=3000	29084.5	944	857	49
	969.5%	31.5%	28.6%	1.6%

Table 2. Number of reconstructed ghost particles, N_p, ghost streaks, N_s, and curved ghost streaks, N_c, for different initial number of particles n and different noise levels, for the case of Hil"s spherical vortex. No constraints are imposed on the reconstruction volume dimensions and maximum allowable displacement. "Ghosts" are the ambiguous reconstructions, while "lost" are the false negatives, which result in losing correct particles during the reconstruction process.

tracer particles are helium-filled soap bubbles (HFSB) generated by an in-house built bubble generator [1] with an updated nozzle design based on the work of [3].

The acquisition frame rate is 1000 fps with an exposure time of 1 ms. The streak images are obtained by summing 60 frames, for an effective "exposure time" of 60 ms. For these measurements, we calibrate the cameras using the pinhole camera model with radial and tangential distortion correction as implemented in the commercial software with which we compare our results. The cameras are synchronized with an external hardware trigger.

Figure 7. View of the experimental setup with two cameras and the vortex generator.

For the streak segmentation we use Mask R-CNN [5]. The streak endpoints are obtained from the single particle frames at t = 0 and t = 60 ms, and they are subsequently assigned to each of the identified masks. For the reconstruction we use an epipolar constraint of d = 1 px. The effective area that is reconstructed from each image has an extent of F = 650×550 px^2, with L = 650 px, as we only reconstruct streaks within this window of interest. The number of reconstructed particles is obtained from the endpoints of all the detected streaks, even if one of their endpoints overlaps.

The streaks, reconstructed with our optimization-based method, can be seen in Fig. 8 in a 3D-view of the domain. The extent of the reconstructed domain is limited to the same range as in the commercial software.

The settings used for the evaluation with the commercial software are the following:

- Allowed triangulation error: 1 voxel
- Minimum track length required: 6 timesteps

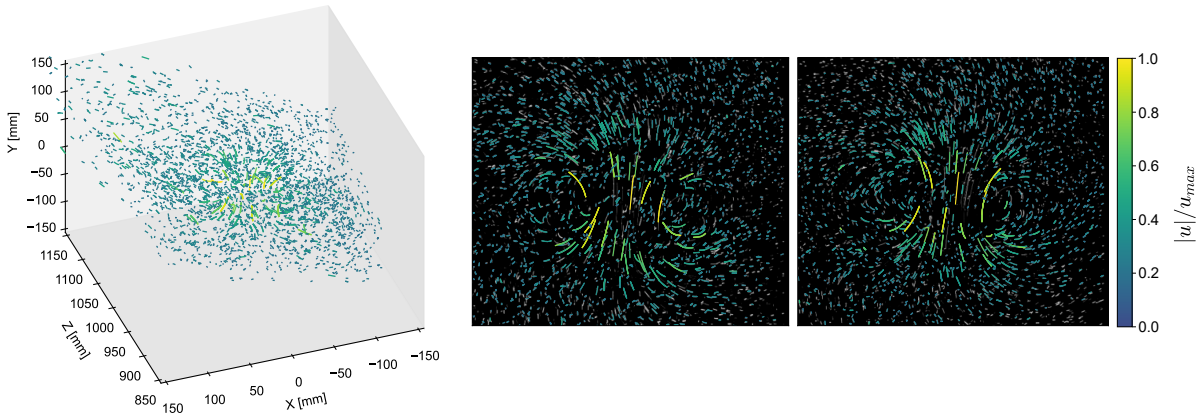

Figure 8. 3D view of the reconstructed streaks and projection on the two camera views. The streaks are reconstructed using our optimization-based method and the settings described above.

- Threshold for 2D particle detection: 1000 counts
- Voxel to mm ratio: 1580 voxels correspond to 400 mm

Acknowledgements

We would like to thank Oliver Häuselmann for developing the vortex generator, and Matthias Machacek for developing the bubble generator used in our experiments. The first author would like to thank Alexander Liniger for helpful discussions.

References

[1] A quantitative Visualization tool for large wind tunnel experiments. *Research Collection*. PhD thesis, 2015. 10

[2] Ayoub B Ayoub. The eccentricity of a conic section. *The College Mathematics Journal*, 34(2):116–121, 2003. 6

[3] Bradley Gibeau and Sina Ghaemi. A modular, 3D-printed helium-filled soap bubble generator for large-scale volumetric flow measurements. *Experiments in Fluids*, 59(12):1–11, 2018. 10

[4] LaVision GmbH. *DaVis 10.1.2*, 2020. 8

[5] Kaiming He, Georgia Gkioxari, Piotr Dollár, and Ross Girshick. Mask R-CNN. In *Proceedings of the IEEE international conference on computer vision*, pages 2961–2969, 2017. 10

[6] Cordelia Schmid and Andrew Zisserman. Geometry and matching of lines and curves over multiple views. *International Journal of Computer Vision*, 40(3):199–233, 2000. 4